MAGNETICALLY COUPLED RESONATORS FOR WIRELESS POWER TRANSMISSION TO INSECT SIZED FLAPPING WING ROBOTS

Johannes M. James[1], Xingyi Shi[2], Joshua R. Smith[2], and Sawyer B. Fuller[1]*
[1]The University of Washington, Mechanical Engineering, Seattle, Washington, USA
[2] The University of Washington, Electrical and Computer Engineering, Seattle, Washington, USA

ABSTRACT

This work reports on progress toward controlled wireless flight of a sub-gram flying insect robot (FIR), powered through a human-safe wireless power transfer method. Previous wireless flights have been powered by light [1, 2] and were not under feedback control. Controlled flight to-date has required a wire tether for actuator drive signals, but a wire greatly diminishes the utility of the robots for envisioned applications such as insect flight research or agricultural support. Obtaining power onboard presents a challenge as available battery technologies do not meet the stringent size, weight, and power (SWaP) constraints of a flying robot weighing slightly more than a toothpick. As a result, obtaining such "power autonomy" for insect sized flying robots remains an open challenge. Our interest in magnetically coupled resonators (MCR) for wireless power transfer is motivated by two significant advantages over laser power beaming: inherent human safety, and the ability to bypass visual obstructions. We report scale-compatible MCR wireless power transfer and a voltage power conversion for piezoelectric actuators that is nearly sufficient to attain liftoff.

KEYWORDS

Wireless Power Transmission, Magnetically Coupled Resonators, Bio-Inspired Robotics, Flying Insect Robot.

INTRODUCTION

Insect sized flying robots represent a frontier of both opportunities and engineering challenges arising from physics scaling effects of shrinking down the characteristic dimensions flying robots. Large numbers of cheap, agile, and low-power robots are envisioned as a promising alternative to few, costly, and power-hungry robotic platforms [3]. Amongst advantageous scaling effects, the large strength-to-weight ratio observed in ants is an important example. But there are other equally advantageous, if less well known, scaling effects we can leverage. These include low total power requirements and the concomitant potential to tap into ambient low-power energy sources such as WiFi [4], high maneuverability, and low materials cost.

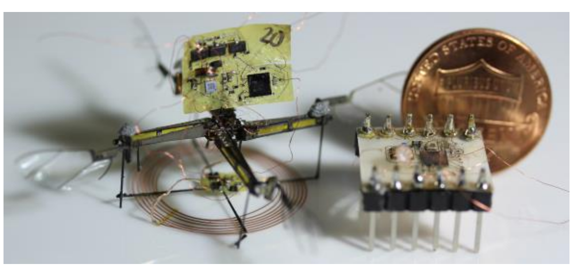

Figure 1: At left is a 4-winged Flying Insect Robot (FIR) similar in design to the 2-winged UW Robofly FIR, with receive coil and fully operational electronics suite for untethered flight. To the right is a testing breakout of a Bluetooth capable MCU planned for future implementation, and a US penny for scale.

While this dream has inspired decades of work since early realizations such as [5, 6], and has separately demonstrated key requirements such as fabrication [7], control [8], sensing [9], controlled flight demonstrations involving piezo-actuated insect-sized robots have all relied on a physical wire tether for control and power signals. This wire tether confounds control and measurements of flight dynamics and nullifies the utility of the robots for envisioned applications such as insect flight research or agricultural support.

Obtaining power onboard presents a challenge as available battery technologies do not meet the stringent size, weight, and power (SWaP) constraints of a flying robot weighing slightly more than a toothpick. The key requirement of power-delivery to an untethered FIR has only been shown utilizing onboard photo-voltaic cells and light sources such as lasers or lamps equivalent to multiple standard suns, posing safety risks or unrealistic levels of illumination [1, 2]. In this work we demonstrate usage of magnetically coupled resonators to deliver power to the FIR safely [19], efficiently, and without needing line of sight. Figure 1. shows the 4-winged FIR platform used in this work developed in [10], which increases payload relative to a 2-winged FIR [11].

Wireless Power Transmission

Given that onboard batteries are not yet feasible, several different methods of wireless power transmission (WPT) were considered to power the Robofly over a range of distance, power capacity, safety, and efficiency. At short range but highly efficient, traditional inductive coupling of coils, as in common-place AC transformers used in AC power distribution worldwide, is limited to very short-range due to the need for a high degree of electromagnetic coupling between non-resonant windings which share a highly permeable magnetic core. While capable of high efficiency, the short operational range and need for a typically heavy magnetic core between coils makes this example of near-field WPT impractical for our FIR. Electromagnetic inductive coupling is also commonly used in wireless charging circuits typical in smartphones or electric toothbrushes. Non-resonant inductive WPT is easy to implement and has adequate power capacity and efficiency for the FIR, but it also requires the receive (Rx) and transmit (Tx) coil to be in close proximity. At higher transmit power inductive coupling also poses safety concerns for humans and equipment due to large electric fields.

On the other hand, far-field radiative power transmission plummets with distance proportional to $1/r^2$ in omni-directional transmission and is unsuitable for powering our FIR during flight. Focused and directional transmission, such as microwave power beaming or phased-array transmission, or laser power beaming [1] targets a receiver and can transmit power wirelessly over great distances and respectable efficiency such as the ~40% efficient PV cells utilized in [1]. However this mode of WPT is highly inefficient if the transmission is not precisely targeted, since electromagnetically radiated power is entirely lost once transmitted. Successful WPT requires precise tracking, nearly perpendicular orientation of the receiver, and clear line-of-sight (LOS). Safety around such radiative WPT systems is difficult to achieve.

Magnetically Coupled Resonators

At an intermediate range, WPT may be achieved using magnetically coupled resonators (MCR) and presents an elegant alternative to the deficiencies of the other WPT options for FIR application. In WPT by MCR, the Tx, Rx, and any intermediate coils, are coupled magnetically and resonate with each other with minimal interaction with other objects. In contrast, inductive coupling can easily induce large electric potentials on nearby objects and human tissue. WPT efficiency via MCR does not depend on extremely high coupling as does inductive WPT. Furthermore, it can operate efficiently even if the coils are far apart and have lower coupling, since energy not taken by the Rx coil largely remains in the high-Q transmitter coil as opposed to be dissipated in space [12]. It is this fundamental difference in operating mechanism that makes MCR WPT safer and more efficient, within transmission range, than radiative WPT. Additionally, the Tx and Rx coils do not require line of sight and the Rx can change position and orientation without the need for the physical tracking and aiming the transmitter required for laser power beaming. Like all WPT methods considered in this work, the Rx must be oriented approximately parallel to the Tx. However, in MCR, misalignment of Tx and Rx coils during flight can be addressed by active frequency tracking and impedance matching handled by the offboard transmitter described in [12, 13], thus the power management of the FIR is passive.

Magnetically coupled resonators for wireless power transmission have demonstrated the capability to power a piezo-actuated cockroach inspired ground microrobot in [14]. In that work the Rx coil weighed 180 mg, roughly three times our weight budget. Nonetheless, this demonstration on a ground robot serves as an intriguing and useful benchmark. As in [16], range of a single Tx, Rx can be efficiently increased for a mobile robot such as the FIR without significant loss of efficiency, by deployment of intermediate passive relay coils.

In this work we choose MCR to obtain power onboard the untethered FIR, using a transmitter similar to [14], and designing our custom Rx coil to fit within the stringent size, weight, and power (SWaP) constraints of the FIR.

FLYING INSECT ROBOT

Robot Mechanical Design

We utilize the 2-winged FIR described in [11] and the similar 4-winged variant developed in [10] and shown in figure 1. These robots use 3-wire bimorph bending beam piezoelectric actuators to actuate wing stroke, while the angle of attack desired for lift results from drag forces against a passive wing hinge during the flapping wing stroke. The wing is flapped at mechanical resonance near 170 Hz, generating enough lift for the robot and approximately 150 mg of additional payload at the achievable voltage from the onboard boost converter and waveform generator. Precise waveform measurements were not performed as wireless voltage and high-side current measurement apparatus is nontrivial and does not fit within the SWaP budget of the untethered robot. However, during benchtop testing the piezoelectric actuator bias and unipolar sinusoid signals were approximately 200 V_{dc} and 170 V_{pp}, and the system including MCU required approximately 250—300 mW input power from the Rx.

Onboard Power Electronics Unit and Actuators

The power electronics unit (PEU) and piezo-electric actuators of the FIR are somewhat analogous to the brain, peripheral nervous system, and musculature of biological insects. The MCU must generate the control signals to operate the flight muscles. In our robot, lightweight high voltage amplifier circuitry on the PEU converts low-voltage power delivered by the Rx coil and power conditioning circuit into the high-voltage signals which cause the piezo-electric actuators to strain and produce mechanical power output by wings. The power conditioning unit attached to the Rx coil has the critical task of converting the power from the Rx coil into forms suitable for both the microcontroller (MCU) and the piezo actuator waveform generator. It does this in lightweight form by a full-wave rectifier (4 diodes since not center-tapped) and voltage regulator. In this work both MCU and high-voltage waveform generator comprise the power electronics unit (PEU) shown atop the FIR in figure 1. The power conditioning circuit was attached directly to the Rx coil and considered separate from the PEU, in keeping with the objective for an interchangeable power source for the FIR. The complete system diagram is shown in figure 2.

Specifically, in our PEU, a half-bridge transistor network was operated with pulse-frequency-modulation (PFM) as a linear amplifier to push and pull the output voltage of the unipolar sinusoidal signal between ground and the ~200V DC bias which our boost converter can achieve in operation. The system diagram is shown in figure 2, and the relation of the basic operation of the low and high sides of the transistor half-bridge to the electrical control signals which result in desired flight control torques are depicted in figure 3.

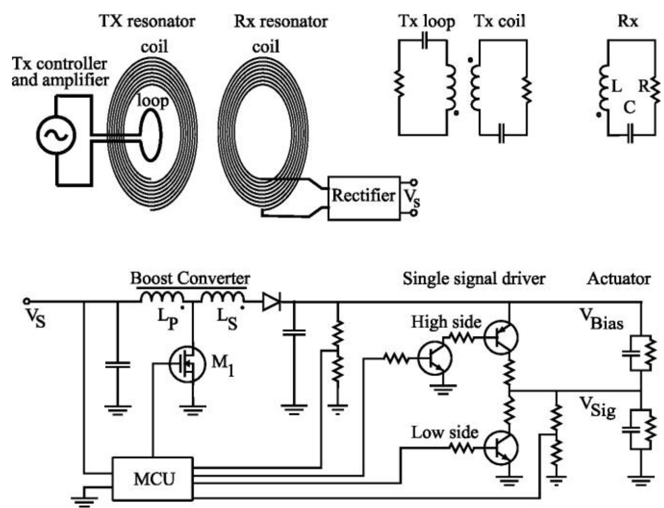

Figure 2: (top left) 3-coil MCR wireless power system with power conditioning circuit at load side. (top right): equivalent circuit of the coupled Tx loop, Tx coil, and series compensated Rx coil. (bottom) Robofly FIR's power electronics unit with one of two signal drivers and piezoelectric bimorph actuator.

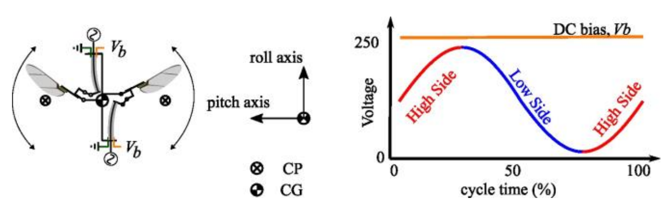

Figure 3: (left) Top view of 2-winged robot showing two bending beam actuators deforming to actuate wing stroke via the 4-bar transmission mechanism. (right) A single unipolar sinusoid and DC bias signal are plotted for a single wing stroke, the red and blue arcs of the unipolar sinusoid indicate the approximate timing of high-side vs low-side, respectively, of the half-bridge amplifier switches.

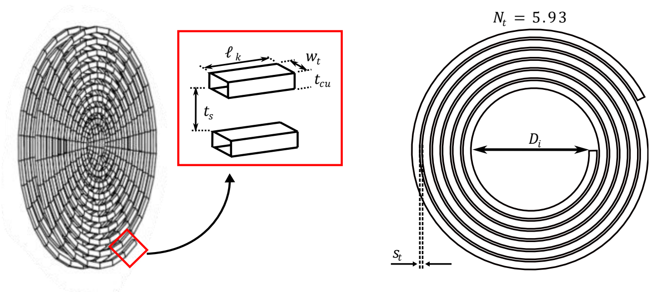

Figure 4: (left) Finite element rendering of a double-sided embedded capacitance Rx coil. Image is adapted from software documentation to illustrate exaggerated substrate thickness. Two conductive trace elements on top and bottom with their thickness t_{cu}, length ℓ_k, and width w_t. The traces are separated by substrate of thickness t_s. (right) 2D vector graphic of a coil used for visualization and manufacture, illustrating the trace separation distance s_t, inner diameter D_i, and number of spiral turns N_t.

RECEIVE COIL DESIGN

Self-Resonant Design

We make use of the inherent parallel-plate capacitance of a double-layered flex PCB material to produce a light-weight inductor with distributed capacitance so as to have a self-resonant frequency near 13.56MHz matched to the MCR transmitter. Resonant tanks are feasible to implement using a single embedded capacitance substrate with traces on both sides, with top and bottom conductive traces connected for series or parallel arrangements of the compensation capacitor C. The system diagram shown in figure 2 depicts one possible arrangement of the coil capacitance C and inductance L. The Rx coil should weigh as little as possible while still having a large diameter for increased range, and the coil's distributed capacitance should not require any additional discrete compensation capacitor to achieve designed resonance – thus minimizing weight and additional power dissipation of the compensation capacitor. Further, this coil should have as high a quality factor Q as possible, so as to extend the range of magnetic coupling [12,17] sufficient for minimum flying power requirements. Thus the resistance of the coil and skin and proximity effects should be minimized. A double-layered spiral design is selected for ease of parametric spiral generation and to achieve trace separation. For the finite element analysis described in further detail below, each spiral was segmented into linear elements with length and width ℓ_k, w_k, as illustrated in figure 4.

Equation (1) gives the self-resonant frequency ω_{SR} in rad/sec of the Rx coil as a function of its capacitance C and inductance L. Equation (2) defines the Rx coil's quality factor Q for a series resonator, with R_{tot} representing the coil's dissipative losses including resistance, skin, and proximity effects. Equation (3) gives the coil's sum total capacitance C, simply equal to the summation over k of each element's conductor area $A_k = w_t\ell_k$, separated by dielectric of thickness t_s and having dielectric constant ϵ. Equation (4) likewise yields the summed weight of the k elements' substrate and copper traces where $A_k, t_s, \rho_s, t_{cu}, \rho_{cu}$ are the cross-sectional area, substrate thickness, substrate density, copper conductor layer thickness, copper density, and substrate dielectric coefficient of each element, respectively.

$$\omega_{sr} = \frac{1}{\sqrt{LC}} \tag{1}$$

$$Q = \frac{1}{R_{tot}}\sqrt{L/C} \tag{2}$$

$$C = \sum_k \left\{\frac{\epsilon A_k}{t_s}\right\} \tag{3}$$

$$m_c = \sum_k \{\rho_s A_k t_s + 2\rho_{cu} A_k t_{cu}\} \tag{4}$$

For modeling fidelity of the parametric spiral coil designs, we obtain the capacitance and weight numerically instead of analytically using the parametrized continuous spiral, in part to stand-in for envisioned finite element solutions to the capacitance along similar lines as the inductance, but also as an inbuilt checkpoint to compare the numerical results to the measured actual capacitance of the continuous analytically generated coil which is ultimately manufactured. Short radius curves and discontinuous turns are undesirable in the traces due to large local electric fields and impedance effects on the Rx coil, and thus we utilized a large number of segments in the finite element representation. We provide no analytical equation for the coil's inductance L or conduction losses R_{tot} coming from resistance and skin and proximity effects, because these are a much more complicated function of the coil's internal electromagnetic interactions, geometry, and material. Thus, while equation (1) can be readily solved for the compensation capacitance required for the desired ω_{SR}, the inductance and lumped resistances including skin effect varies simultaneously and are less trivial to predict for arbitrary Rx morphologies. While some analytical formulae for inductance and conduction losses are stated in [18] and provide high accuracy starting points to coil parameters for optimal analytic design, any modeling errors disproportionately impact the down-scaled coil needed for the FIR. Therefore in this work we explore automated finite element analysis for this multivariate optimization problem. The subsection below describes how we numerically solve the inductance L and high-frequency impedance characteristics as part of the Rx coil design.

Optimization

We performed an optimization of the coil parameters $P = \{D_i, N_t, w_t, s_t, \epsilon, t_{cu}, t_s\}$. These are the spiral inner diameter, number of turns, coil trace width, trace spacing, the substrate dielectric constant, the substrate thickness, and conductor thickness, respectively. Inner diameter is a less-typical coil measure than nominal diameter but D_i is varied in this work as a convenient starting point for coil segmentation and since nominal coil diameter and outer diameter are constrained according to N_t, s_t. The Rx coil in a MCR WPT system must have high quality factor Q and resonate at the designed frequency in order to magnetically couple over meaningful distance to the Tx. The Rx coil on this robot in particular must be both light-weight and provide sufficient power output to the PEU at range. Since range, efficiency, coupling, and power transfer capacity are also dependent on the ratio of Rx and Tx coil diameters, the design must strike a balance between competing goals of high Q and power capacity vs. low weight, despite the resonance exhibiting high degree of sensitivity to all of the parameters enumerated above. In this work we utilize a gradient descent optimization routine to design the set of parameters P, given the complexity of the design space.

Guided by analytical Rx coil design principals stated in [18] and basic equations above, we develop and minimize a simple cost function J; a weighting vector W which assigns relative importance of the metrics for coil weight, natural frequency, total inductance, and quality factor Q of a coil; vector X quantifying the coils' computed mass and electrical properties, and we determine the set of parameters to vary. The construction of vectors X and penalty weights W represent an engineering judgment call between the tradeoffs of total Rx coil weight and quality factor, as a higher Q with higher power transfer capacity corresponding to inductance L, competes with the interest of low weight. The cost function J minimized in equation 7 provides us a scalar metric for each candidate coil design. This cost is then minimized by gradient descent as in equation 7 to yield locally optimal candidate coil $C_{Rx}(P)$.

$$W = \mathrm{diag}\left[j_m, j_\omega, j_L, j_Q\right] \tag{5}$$

$$X = \left[m_c,\ |\omega_{Tx} - \omega_{SR}|, \frac{1}{L}, \frac{1}{Q}\right]^T \tag{6}$$

$$C_{Rx} = \min_P\{J\} = \min_P\{X^T W X\} \tag{7}$$

Where j_m, j_ω, j_L, j_Q are the weighting terms for total coil weight, natural frequency, inductance, and quality factor, respectively. ω_{Tx} is the operating frequency for transmission which is selected similarly as in [12] for coupling range, minimizing undesired magnetic interactions with surroundings, and Tx control via active frequency tracking and impedance matching. To provide an educated starting guess for appropriate weights, the weights were normalized to characteristics of coils from [14, 18] assumed to be approximately optimal, and the algorithm will converge to more optimal values for the FIR if possible.

Since the cost function of the multi-variate coil design is unknown but assumed nonconvex, multiple starting points for coils across the design space, e.g. large coils, skinny coils, range of spiral arc, trace spacing, etc, are chosen as starting points; ensuring that the optimization does not get stuck in sub-optimal local minima. In particular, we found that Rx coil Q and m_c were particularly sensitive to coil diameter and trace-width, and thus we iterated starting conditions across the full range of these variables. Other important design variables such as substrate thickness, different options of substrate with different dielectric constants, series vs. parallel connection and multiple coil layers, and copper cladding thickness are not suitable for continuous variation by the gradient descent, so gradient descent was performed within each of these sets of discrete options in order to formulate a comprehensive set of candidate designs.

IMPLEMENTATION

Automated Optimization and CAD

We implemented gradient descent of equation 7 using a custom Python script. During each candidate coil descent, the program varied coil design parameters from an initial guess P_0, generated a design file detailing the finite element model, called FastHenry 3D inductance solver [20], evaluated the resulting inductance analysis file, and chose the optimal parameter variation for subsequent descent iterations while saving locally optimal design candidates.

The FastHenry solver utilizes a 3D specification of geometry and properties of the coil whose finite elements (segments) of the coil are defined by the Python script and encoded into a template inductor file. A FastHenry rendering of a segmented coil design for the finite element analysis is shown in figure 4. The results of the inductance analyses were parsed and used to compute the cost gradient, and the algorithm chose the best available variable change and began a subsequent iteration. If the cost gradient converged to a low value then the optimization ceased and the coil design was chosen as a locally optimal candidate. Amongst locally-optimal candidate Rx coil designs, several designs featuring lowest cost were used by the same program to generate a scalable vector graphics file for visualization and a CAM file for manufacture.

Manufacture and Testing

Manufacture was done using 355nm frequency-tripled Nd:YAG Diode Pumped Solid State Laser (DPSS) micro-machining system, the same equipment used to fabricate the PEU flex PCB and the robot chassis. The Rx coils were realized by two methods: Firstly, spray polyurethane PCB etch resist was rastered off the double-clad flex PCB material by DPSS laser, then unwanted copper removed by chemical etchant. This raster-etch (RETCH) process is used for in-house fabrication of the PEU flex circuits as well, but a coil fabricated this way still has a large area of the material's bare substrate which serves to maintain the coil shape, but does not contribute electrically and adds $20-50\%$ additional weight. Additionally, over-etching the RETCH'ed coil potentially caused deviation from design parameters. In the second method, we directly through-cut the coil design from the embedded capacitance flex PCB material. The second method was preferred for lighter weight but required insulated carbon fiber support rods to span the coil and maintain the precise designed shape as well as provide mounting points for robot assembly. In both methods, fabrication inaccuracy of the photo machining due to DPSS laser spot diameter of $20\mu m$, imprecision of the photo machining vector path planning, and xy positioning error of laser scanning was assumed to be negligible.

While several candidate designs were implemented using the 3M C2006 embedded capacitance material with $6\mu m$ substrate and $35\mu m$ copper thickness, it was found that the copper adherence to substrate made the material delicate to handle and susceptible to tearing and delamination, ruining the coil. Polyimide substrates from the DuPont Pyralux series with $12\mu m - 25\mu m$ substrate thickness and $12\mu m - 25\mu m$ copper trace thickness were also found to have suitable dielectric constant with similar degrees of repeatability but superior copper adhesion. Thus in this work we favored the Pyralux flex PCB material used in our PEU fabrication.

Manufactured candidate coils were tested using an LCR meter to confirm designed inductance, capacitance, and resistance. The coils were then adhered to insulated support structure, and attached to the power conditioning circuit by Litz wire approaching at perpendicular to the coil, so as to minimize unintended magnetic interactions with the WPT. An assembled coil and power conditioning circuit is shown in figure 2.

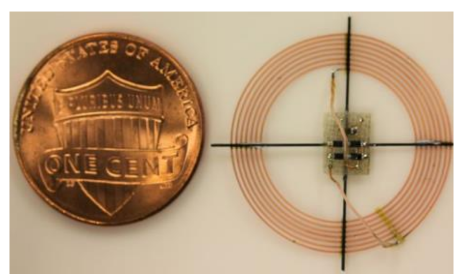

Figure 5: Rx coil and power conditioning circuit mounted to carbon fiber rods, shown next to a US penny for scale.

RESULTS AND DISCUSSION

Assembled robots for untethered experiments were constructed in 2-wing and 4-wing variants, with several selections of optimized candidate coils. Table 1 shows the weights of the systems.

Table 1: Weight of robot systems.

System	***Measured Weight***
4-wing robot (airframe, wings, and actuators)	143 mg
2-wing robot (airframe, wings, and actuators)	90 mg
Power-electronics unit (PEU) with microcontroller	88 mg
Receive coil on embedded capacitance flex-PCB	31 mg
Power conditioning circuit	9 mg
Fully assembled 2-wing robot	218

Figure 6 shows how the scattering parameter $|S_{21}|$ varies with distance between Tx and Rx coils. The $|S_{21}|$ parameter is an indicator of the wireless power efficiency that the coil system can achieve, as measured by vector network analyzer (VNA). The optimized Tx had a diameter of $\mathbf{30}$ cm. Our results show a decreased $|S_{21}|$ at close range to the Tx. In practice, the drop of the coil efficiency at this over-coupled regime can be mitigated by the Tx controller, which employs active impedance matching and frequency tuning to compensate for the changing coupling as the Tx moves [16]. The total received power must be a minimum for flight, and so distances too great to deliver minimal power for flight were not plotted even though power is still available and could potentially be utilized for non-flying robot tasks such as passive sensing or recharging.

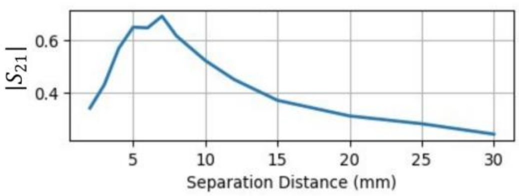

Figure 6: The measured scattering parameter $|S_{21}|$ diminishes with distance. Decreased efficiency at lower distance is compensated by active frequency tracking and impedance matching.

Figure 7: Still-frames of a fully assembled 4-wing robot recording flapping its wings powered wirelessly at up to 1.25 inch distance from Tx coil located underneath the acrylic platform. (right) the robot is gripped by tweezers and lifted above the platform, still receiving enough power to wake the PEU and flap the wings. Here, the 51-AWG wire tether we used for measurement and programming has been cut.

Figure 7 shows the fully untethered FIR powered by the Rx coil, with transmitter placed approximately $\mathbf{25}$mm underneath the acrylic surface. Lift was enough to move across the surface but not to take off. Our design and simulation predicted slightly higher $|S_{21}|$ than achieved in the best performing coils. The primary hindrance to sustained flight in this case was limitations in the PEU efficiency and FIR wear. More generally, the Rx coil design is difficult to achieve in practice since the capacitance and self-resonance of the ultra-light Rx coil are extraordinarily sensitive to the parameters of coil design such as dielectric properties which can be impacted by manufacturing variability, soldering heat or pinching during assembly, excessive solder, heat during operation, or flexing and vibration. For example, assuming uncorrelated changes to L and R, even small δC variations in capacitance, $C = C_{nominal} \pm \delta C$, significantly impact Q , especially given low nominal values of L, C obtainable with SWaP budget of the FIR Rx coil. It is possible that smearing of the traces across the dielectric impacted the coils as well. This can be caused by laser through-cutting of the coils leaving microdeposits of conductor spanning the dielectric where cut, a phenomenon similarly impacting piezoelectric actuator fabrication during laser micro-machining.

Regarding heat dissipation, several hundred mW of power are received by the Rx coil during the WPT flight experiments, which represents a large power density. Since the coil must be light, there is both minimal conductor surface area available to cool the coil and little thermal capacitance to begin with. Resulting temperature fluctuations may change the electrical properties of the coil, adversely impacting the high quality factor Q needed for MCR WPT.

CONCLUSIONS AND FUTURE WORK

The coil design process can be meaningfully improved in several ways. Firstly, simulating coupling to Tx and relay coils in addition to the rx. and utilizing finite element analysis of the capacitance of the rx coil to supplement the analytical calculation would improve accuracy**.** Incorporating fine element analysis of parasitic capacitance was not done in this work but would be particularly useful to optimize around skin and proximity effects. Lastly, the cost function can readily be augmented with additional or alternative metrics for particular designs, e.g. including expressions in X along with corresponding weights in W which would penalize design sensitivity to uncertainty in parameters, or terms which are more directly related to impedance and power capacity of the Rx.

WPT using MCR is shown to work to power the robot sufficiently to flap the wings and nearly take off despite inefficiency in the power electronics, actuator breakage, and undesired torque biases in the robot during flapping which reduced lift. A more power efficient power electronics within the SWaP budget of FIRs is an ongoing design effort which will unlock successful demonstration of FIR powered by MCR. Regardless, MCR power worked impressively on a robot too small to carry batteries and represents perhaps the lightest demonstration of this human-safe approach yet. Additionally, the Rx coil itself provides incidental benefits such as shielding the wings from collision and easing the burden of flight control somewhat by adding lightweight angular inertia to the otherwise very fast dynamics of the FIR. We anticipate that only a few refinements will be necessary to attain free-flight under this form of WPT.

ACKNOWLEDGEMENTS

A wireless power transmitter from Wibotic Inc. was used in this research. Disclosure: J.R. Smith is a Wibotic co-founder and shareholder.

REFERENCES

[1] James, Johannes, et al. "Liftoff of a 190 mg laser-powered aerial vehicle: The lightest wireless robot to fly." 2018 IEEE International Conference on Robotics and Automation (ICRA). IEEE, 2018.

[2] Jafferis NT, Helbling EF, Karpelson M, Wood RJ. "Untethered flight of an insect-sized flapping-wing microscale aerial vehicle", *Nature*. 2019 Jun 27;570(7762):491-5.

[3] Brooks, Rodney A., and Anita M. Flynn. *Fast, cheap and out of control* 1989.

[4] Talla, Vamsi, et al. "Powering the next billion devices with Wi-Fi", Proceedings of the 11th ACM Conference on Emerging Networking Experiments and Technologies. 2015.

[5] FEARING RS. "Toward micromechanical flyers", In Frontiers of Engineering: Reports on Leading-Edge Engineering from the 2001 NAE Symposium on Frontiers of Engineering 2002 Sep 10 (p. 21). National Academies Press.

[6] Wood RJ. The first takeoff of a biologically inspired at-scale robotic insect. *IEEE transactions on robotics*. 2008 Apr 4;24(2):341-7.

[7] Whitney JP, Sreetharan PS, Ma KY, Wood RJ. "Pop-up book MEMS", *Journal of Micromechanics and Microengineering*. 2011 Oct 14;21(11):115021.

[8] Ma KY, Chirarattananon P, Fuller SB, Wood RJ. "Controlled flight of a biologically inspired, insect-scale robot", *Science*. 2013 May 3;340(6132):603-7.

[9] Fuller SB, Helbling EF, Chirarattananon P, Wood RJ. "Using a mems gyroscope to stabilize the attitude of a fly-sized hovering robot", InIMAV 2014: International Micro Air Vehicle Conference and Competition 2014, Delft, The Netherlands, August 12-15, 2014 2014 Aug 12. Delft University of Technology.

[10] Fuller SB. "Four wings: An insect-sized aerial robot with steering ability and payload capacity for autonomy", *IEEE Robotics and Automation Letters*. 2019 Jan 6;4(2):570-7.

[11] Chukewad YM, James J, Singh A, Fuller S. "RoboFly: An insect-sized robot with simplified fabrication that is capable of flight, ground, and water surface locomotion", *IEEE Transactions on Robotics*. 2021 May 31;37(6):2025-40.

[12] Sample AP, Meyer DT, Smith JR. "Analysis, experimental results, and range adaptation of magnetically coupled resonators for wireless power transfer", *IEEE Transactions on industrial electronics* 2010 Mar 22;58(2):544-54.

[13] Waters BH, Sample AP, Smith JR. "Adaptive impedance matching for magnetically coupled resonators", *Prog Electromagn Res*. 2012 Aug 19:694-701.

[14] Karpelson M, Waters BH, Goldberg B, Mahoney B, Ozcan O, Baisch A, Meyitang PM, Smith JR, Wood RJ. "A wirelessly powered, biologically inspired ambulatory microrobot" In 2014 IEEE International Conference on Robotics and Automation (ICRA) 2014 May 31 (pp. 2384-2391). IEEE.

[15] Casanova JJ, Low ZN, Lin J. "A loosely coupled planar wireless power system for multiple receivers", *IEEE Transactions on Industrial Electronics*. 2009 Jun 5;56(8):3060-8.

[16] Shi X, Smith JR. "Reconfigurable and adaptive coupled relay resonator platform for a moving receiver", In 2019 International Workshop on Antenna Technology (iWAT) 2019 Mar 3 (pp. 182-185). IEEE.

[17] Kurs A. " Wireless Power Transfer via Strongly Coupled Magnetic Resonance," 7, 10.1126, *science*. 1143254. 2007.

[18] Waters BH, Mahoney BJ, Lee G, Smith JR. Optimal coil size ratios for wireless power transfer applications. In 2014 IEEE international symposium on circuits and systems (ISCAS) 2014 Jun 1 (pp. 2045-2048). IEEE.

[19] Christ A, Douglas MG, Roman JM, Cooper EB, Sample AP, Waters BH, Smith JR, Kuster N. "Evaluation of wireless resonant power transfer systems with human electromagnetic exposure limits" *IEEE Transactions on Electromagnetic compatibility*. 2012 Oct 25;55(2):265-74.

[20] Kamon M, Tsuk MJ, White J. "FASTHENRY: A multipole-accelerated 3-D inductance extraction program", In Proceedings of the 30th international design automation conference 1993 Jul 1 (pp. 678-683).

CONTACT

J.M. James, JMJames@uw.edu